Biomedical Optics EXPRESS

Towards a bimodal proximity sensor for in situ neurovascular bundle detection during dental implant surgery

Jessie R. Weber,[1,*] François Baribeau,[1] Paul Grenier,[1] Frédéric Émond,[1] Sylvain Dubois,[1] François Duchesne,[1] Marc Girard,[1] Timothy Pope,[1] Pascal Gallant,[1] Ozzy Mermut,[1] and Hassan Ghaderi Moghadam, D.D.S., MSc, FRCD(C)[2]

[1]*Institut national d'optique (INO), 2740 rue Einstein, Québec, QC G1P 4S4, Canada*
[2]*The Ottawa Hospital, 3409 Carling Avenue, Ottawa, ON K2H 7V5, Canada*
[*]*jessie.weber@ino.ca*

Abstract: Proof of concept results are presented towards an *in situ* bimodal proximity sensor for neurovascular bundle detection during dental implant surgery using combined near infrared absorption (NIR) and optical coherence tomography (OCT) techniques. These modalities are shown to have different sensitivity to the proximity of optical contrast from neurovascular bundles. NIR AC and DC signals from the pulsing of an artery enable qualitative ranging of the bundle in the millimeter range, with best sensitivity around 0.5-3mm distance in a custom phantom setup. OCT provides structural mapping of the neurovascular bundle at sub-millimeter distances in an *ex vivo* human jaw bone. Combining the two techniques suggests a novel ranging system for the surgeon that could be implemented in a "smart drill." The proximity to the neurovascular bundle can be tracked in real time in the range of a few millimeters with NIR signals, after which higher resolution imaging OCT to provide finer ranging in the sub-millimeter distances.

OCIS codes: (170.0170) Medical optics and biotechnology; (170.1850) Dentistry; (170.1610) Clinical applications; (170.4500) Optical coherence tomography; (170.6510) Spectroscopy, tissue diagnostics.

References and links

1. C. E. Misch, *Contemporary Implant Dentistry* (Elsevier Health Sciences, 2007).
2. Millenium Research Group report: *US Markets for Dental Implants*, 2006.
3. G. A. Zarb and A. Schmitt, "The longitudinal clinical effectiveness of osseointegrated dental implants: The Toronto study. Part III: Problems and complications encountered," J. Prosthet. Dent. **64**(2), 185–194 (1990).
4. G. Poirot, J. F. Delattre, C. Palot, and J. B. Flament, "The inferior alveolar artery in its bony course," Surg. Radiol. Anat. **8**(4), 237–244 (1986).
5. C. Kilic, K. Kamburoğlu, T. Ozen, H. A. Balcioglu, B. Kurt, T. Kutoglu, and H. Ozan, "The position of the mandibular canal and histologic feature of the inferior alveolar nerve," Clin. Anat. **23**(1), 34–42 (2010).
6. C. E. Misch and R. Resnik, "Mandibular Nerve Neurosensory Impairment After Dental Implant Surgery: Management and Protocol," Implant Dent. **19**(5), 378–386 (2010).
7. M. Choi, M. O. Culjat, R. S. Singh, and S. N. White, "Ultrasound imagery for dental implant diagnosis and treatment planning in a porcine model," J. Prosthet. Dent. **108**(6), 344–353 (2012).
8. D. A. Tyndall, J. B. Price, S. Tetradis, S. D. Ganz, C. Hildebolt, and W. C. Scarfe; American Academy of Oral and Maxillofacial Radiology, "Position statement of the American Academy of Oral and Maxillofacial Radiology on selection criteria for the use of radiology in dental implantology with emphasis on cone beam computed tomography," Oral Surg Oral Med Oral Pathol Oral Radiol **113**(6), 817–826 (2012).
9. C. Xiaojun, Y. Ming, L. Yanping, W. Yiqun, and W. Chengtao, "Image guided oral implantology and its application in the placement of zygoma implants," Comput. Methods Programs Biomed. **93**(2), 162–173 (2009).
10. G. Greenstein and D. Tarnow, "The mental foramen and nerve: clinical and anatomical factors related to dental implant placement: a literature review," J. Periodontol. **77**(12), 1933–1943 (2006).
11. T. Renton, "Minimising and managing nerve injuries in dental surgical procedures," Faculty Dental Journal, King's College London, **2**(4) (October 2011).

#197910 - $15.00 USD Received 19 Sep 2013; revised 15 Nov 2013; accepted 18 Nov 2013; published 2 Dec 2013

12. A. Elayouti, R. Weiger, and C. Löst, "The ability of root ZX apex locator to reduce the frequency of overestimated radiographic working length," J. Endod. **28**(2), 116–119 (2002).
13. Y. Mendelson, "Pulse Oximetry: Theory and Applications for Noninvasive Monitoring," Clin. Chem. **38**(9), 1601–1607 (1992).
14. J. L. Reuss and D. S. Siker, "The pulse in reflectance pulse oximetry: modeling and experimental studies," J. Clin. Monit. Comput. **18**(4), 289–299 (2004).
15. A. M. Zysk, F. T. Nguyen, A. L. Oldenburg, D. L. Marks, and S. A. Boppart, "Optical coherence tomography: a review of clinical development from bench to bedside," J. Biomed. Opt. **12**(5), 051403 (2007).
16. S. R. Chinn, E. A. Swanson, and J. G. Fujimoto, "Optical coherence tomography using a frequency-tunable optical source," Opt. Lett. **22**(5), 340–342 (1997).
17. M. E. Brezinski, G. J. Tearney, B. E. Bouma, J. A. Izatt, M. R. Hee, E. A. Swanson, J. F. Southern, and J. G. Fujimoto, "Optical coherence tomography for optical biopsy. Properties and demonstration of vascular pathology," Circulation **93**(6), 1206–1213 (1996).
18. N. Tachikawa, R. Yoshimura, K, Ohbayashi, "Cross-sectional imaging of extracted jawbone of a pig by optical coherence tomography," Proc. SPIE **7884**, Lasers in Dentistry XVII (2011).
19. L. Spinelli, M. Botwicz, N. Zolek, M. Kacprzak, D. Milej, A. Liebert, U. Weigel, T. Durduran, F. Foschum, A. Kienle, F. Baribeau, S. Leclair, J. Bouchard, I. Noiseux, P. Gallant, O. Mermut, A. Pifferi, A. Torricelli, R. Cubeddu, H. Ho, M. Mazurenka, H. Wabnitz, K. Klauenberg, O. Bodnar, C. Elster, M. Bénazech-Lavoué, Y. Bérubé-Lauzière, F. Lesage, P. Di Ninni, F. Martelli, and G. Zaccanti, "Inter-Laboratory Comparison of Optical Properties Performed on Intralipid and India Ink," in *Biomedical Optics and 3-D Imaging*, OSA Technical Digest (Optical Society of America, 2012), paper BW1A.6.
20. A. Pifferi, A. Torricelli, P. Taroni, A. Bassi, E. Chikoidze, E. Giambattistelli, and R. Cubeddu, "Optical biopsy of bone tissue: a step toward the diagnosis of bone pathologies," J. Biomed. Opt. **9**(3), 474–480 (2004).
21. N. Ugryumova, S. J. Matcher, and D. P. Attenburrow, "Measurement of bone mineral density via light scattering," Phys. Med. Biol. **49**(3), 469–483 (2004).
22. V. V. Tuchin, *Tissue Optics* (SPIE Press, 2007).
23. S. Prahl, "Tabulated Molar Extinction Coefficient for Hemoglobin in Water," *http://omlc.ogi.edu/spectra/hemoglobin/summary.html*, (1998).
24. M. L. Vernon, J. Freàchette, Y. Painchaud, S. Caron, and P. Beaudry, "Fabrication and Characterization of a Solid Polyurethane Phantom for Optical Imaging Through Scattering Media," Appl. Opt. **38**(19), 4247–4251 (1999).
25. J. P. Bouchard, I. Veilleux, R. Jedidi, I. Noiseux, M. Fortin, and O. Mermut, "Reference optical phantoms for diffuse optical spectroscopy. Part 1--Error analysis of a time resolved transmittance characterization method," Opt. Express **18**(11), 11495–11507 (2010).
26. P. Studinger, Z. Lénárd, Z. Kováts, L. Kocsis, and M. Kollai, "Static and dynamic changes in carotid artery diameter in humans during and after strenuous exercise," J. Physiol. **550**(2), 575–583 (2003).
27. D. Boas, C. Pitris, and N. Ramanujam, *Handbook of Biomedical Optics* (Taylor & Francis, 2011).
28. N. Stuban, M. Niwayama, and H. Santha, "Phantom with Pulsatile Arteries to Investigate the Influence of Blood Vessel Depth on Pulse Oximeter Signal Strength," Sensors (Basel) **12**(12), 895–904 (2012).

1. Introduction

Dental implants are a widely accepted treatment for the partially or completely edentulous patient, with over 1 million implants inserted annually in the United States and that rate is expected to increase at a sustained growth of 12-15% for the next several years [1,2]. The basic implant procedure involves using a drill to create an osteotomy in the bone where a titanium screw is placed. A dental prosthesis is then placed onto the frame of the titanium screw. The success of these procedures, however, is dependent on effective osseointegration, defined as anchorage by the formation of bony tissue around the implant, such that implant shows no mobility when loaded. Major factors for the successful integration of the implant depend on the type of jaw treated, the density of the bone, and the length and depth of the implant [3]. An additional challenge is that once a tooth has been extracted the bone resorbs and leaves less tissue available for an appropriate length of implant. The choices to circumvent this are either extensive vertical bone grafting, which is highly unpredictable and has inherit risks, or moving the nerve out of the jaw, or "nerve lateralization," which also carries a high risk of nerve injury and sometimes permanent damage.

Implant depth is determined by the surgeon when drilling the channel in the mandible. The depth when drilling a dental implant channel within the mandible is limited by the risk of breaching the mandibular canal, shown in Fig. 1(A) and shown in cross section in Fig. 1(B), that contains a neurovascular bundle including the inferior alveolar nerve (IAN), which terminates as the mental nerve providing sensory enervation to the lower lips and chin, and its

#197910 - $15.00 USD Received 19 Sep 2013; revised 15 Nov 2013; accepted 18 Nov 2013; published 2 Dec 2013

corresponding artery and vein (for detailed anatomy, see Poirot, et al, 1986 [4] and Kilic, et al, 2010 [5]). Loss of sensation in the anterior mandible, such as paresthesia or numbness to the lower lip and chin, can occur due to the disruption of the IAN. The reported incidence of nerve injury from implant placement in the literature is highly variable and ranges depending on the study from 0% to as high as 44%, with 73% of dentists encountering neurosensory impairment within their practice [6].

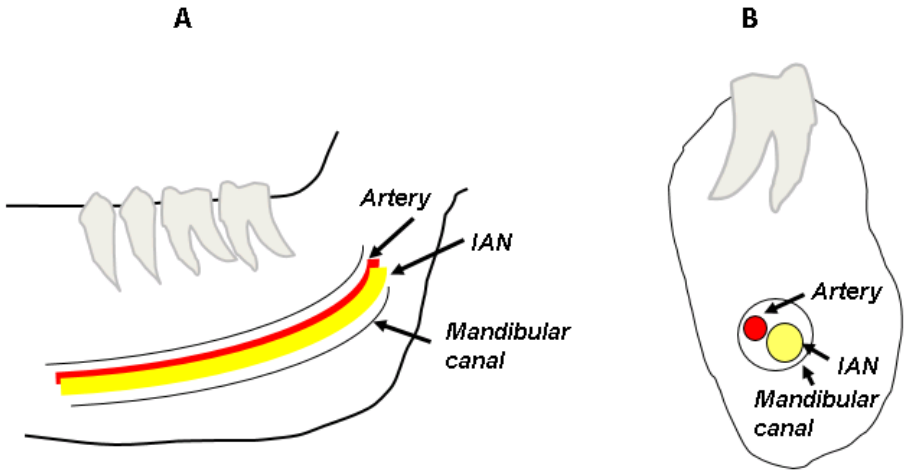

Fig. 1. (A) The mandibular canal shown within the mandible, containing the neurovascular bundle, and (B) A cross section of view of the mandible showing the neurovascular bundle within the canal.

There are no real-time methods to localize the IAN during dental surgery. Although ultrasound could provide real-time monitoring, its lack of ability to penetrate beyond bony surfaces allows it only to monitor the soft tissues above implant sites [7]. Currently, only preoperative imaging methods are available to surgeons for determining the position of the IAN. 2D intraoral radiography is the most widely used and least costly technique, however suffers from low resolution and no ability to visualize the cross-sectional anatomy. Panoramic tomography and Computed Tomography (CT) are both 3D methods, but also suffer from low resolution. In addition, CT scans are relatively costly and typically only available in hospitals and medical centers. Cone beam computed tomography (CBCT) provides 3D images with higher resolution, but is less frequently available and more costly. The American Academy of Oral and Maxillofacial Radiology recommends the use of panoramic radiography for initial evaluation of implant patients, but considers it inadequate for preoperative planning, and recommends that "CBCT should be considered as the imaging modality of choice for preoperative cross-sectional imaging of potential implant sites" [8].

Pre-surgical CT scans used for image guided surgery typically achieve a resolution accuracy of less than 2mm [9]. This uncertainty, combined with placement error, leaves the surgeon to err on the side of caution, with recommendations to leave a "safety zone" of at least 2mm from the inferior alveolar canal, with many practitioners recommending at least 4mm [10, 11]). This "safety zone" ensures implant placements at depths that will not exceed imaging and placement error. However, a clear tradeoff exists between leaving a minimal "safety zone" and maximizing the depth of the implant for best osseointegration.

There is thus a need to develop a tool that is able to detect the proximity of the drill to the IAN during implant procedures. This tool should allow the drill to approach closely, but not impair or damage the IAN within an acceptable error limit of the mandibular canal. We propose a bimodal 'smart drill,' a combination of two optical techniques integrated into a

#197910 - $15.00 USD Received 19 Sep 2013; revised 15 Nov 2013; accepted 18 Nov 2013; published 2 Dec 2013

fiber probe format envisioned small enough to fit within a dental surgery drill bit for real time, non-invasive proximity sensing during the implant procedure. The electronic apex locator revolutionized endodontics, enabling more accurate and predictable assessment of working length during root canals [12]. A 'smart drill' concept, as proposed here and seen in Fig. 2, could do the same for dental implantology. Below, we present proof of concept results of both optical techniques' sensitivity to the proximity of a neurovascular bundle and a concept of operation using that sensitivity to guide dental and other similar implantology procedures in real time.

1.1 NIR

Tissue at NIR wavelengths can be characterized by its optical absorption and scattering properties. Absorption properties come from tissue chromophores, like oxy- and de-oxyhemoglobin, that have distinct absorption spectra. Scattering come from refractive index differences related to tissue structure, with bulk scattering properties resulting from cellular and organelle membranes, as well as fibrous structures such as intra- and extra-cellular matrix. In pulse oximetry, the NIR absorption properties of blood can be used dynamically to isolate a signal from a pulsating artery. When an artery pulses, its volume changes periodically. Since arterial blood has higher optical absorption than the tissue surrounding it, these volume changes are optically detectable. Pulse oximetry locks onto this changing signal at two wavelengths, one with a larger component of oxyhemoglobin absorption and one with greater deoxyhemoglobin absorption, dividing out the static information (unchanging tissue properties) to isolate the ratio of oxy- to deoxy-hemoglobin, resulting in a measure of the arterial oxygen saturation. Pulse oximeters are typically calibrated to empirical data with known oxygen saturation [13].

In the case of sensing the proximity to an artery, as the optical probe approaches the pulsing artery, the signal of both the AC pulse strength [14] and DC optical signal are expected to change. The AC signal should be at a maximum at a distance just far enough from the pulse that the volume change induced by the pulse creates the maximum optical change. From there, the AC signal is expected to decrease as the probe moves further away from the artery, since the surrounding static tissue properties will further and further mask the arterial signal. The DC signal comes from the steady-state artery and surrounding tissue properties. Since the blood in the artery is much more absorbent than the surrounding tissue, the DC signal should increase as the probe moves away from it – the surrounding tissue's less absorbent nature allows more photons to return to the probe. As a result, the DC signal will be at a maximum far from the artery, where the probe sees only the surrounding tissue, and then will decrease as the artery comes into the probe's interrogation volume. The AC and DC versus distance signals therefore provide separate sources of sensitivity to artery proximity. These signals can either be used to sense relative proximity to the neurovascular bundle, or calibrated to provide quantitative distance. However, for precise placement with fine resolution and imaging capability very close to the IAN, OCT is required (see Section 1.2 below).

1.2 OCT

OCT has proven to be an excellent solution for *in vivo* medical imaging and optical biopsy for a wide range of clinical applications [15]. Swept-Source OCT (SS-OCT) is one of the more successful techniques among OCT schemes, offering higher sensitivity with better penetration depth than other types of OCT systems [16]. OCT provides structural information directly, similar to a B-mode ultrasound image but optically and with higher resolution. OCT has previously been demonstrated to see over 1.5mm deep in the cortical bone of an *in vitro* human clavicle [17]. Preliminary work has also shown potential for deeper penetration in jaw bone in a porcine model using longer wavelengths (1600-1638nm), perhaps up to 3mm, although the work was based on drop-off of optical signal through thick sections of bone

#197910 - $15.00 USD Received 19 Sep 2013; revised 15 Nov 2013; accepted 18 Nov 2013; published 2 Dec 2013

rather than measurement of a feature or surface at that depth [18]. The technique could theoretically visualize the IAN directly, compared to indirect identification of the neurovascular bundle with NIR absorption from the blood vessel. OCT only requires one parameter to be known a priori to extract quantitative distance, the tissue refractive index. In the case of the application targeted here, an OCT probe could be envisioned as operating in a one-dimensional implementation A-mode (point measurement), or two-dimensional B-mode (scanning). One possible limitation is the achievable contrast between various tissue types. However, the main limitation envisioned to the performance of such a device is detection range. OCT can provide an excellent axial resolution (~10 μm) at shallow depths, in the range of <1-1.5 mm and depending on tissue optical properties. It could therefore provide good precision on the position of the IAN at close distances only. Both the fine axial resolution capability and the imaging capability could lend themselves ideally to final positioning of the drill. While OCT can provide fine resolution and imaging capability at short distances, the NIR technique is required to bring the drill to within the "safety zone" of 2-4mm, as described in Section 1.1, above.

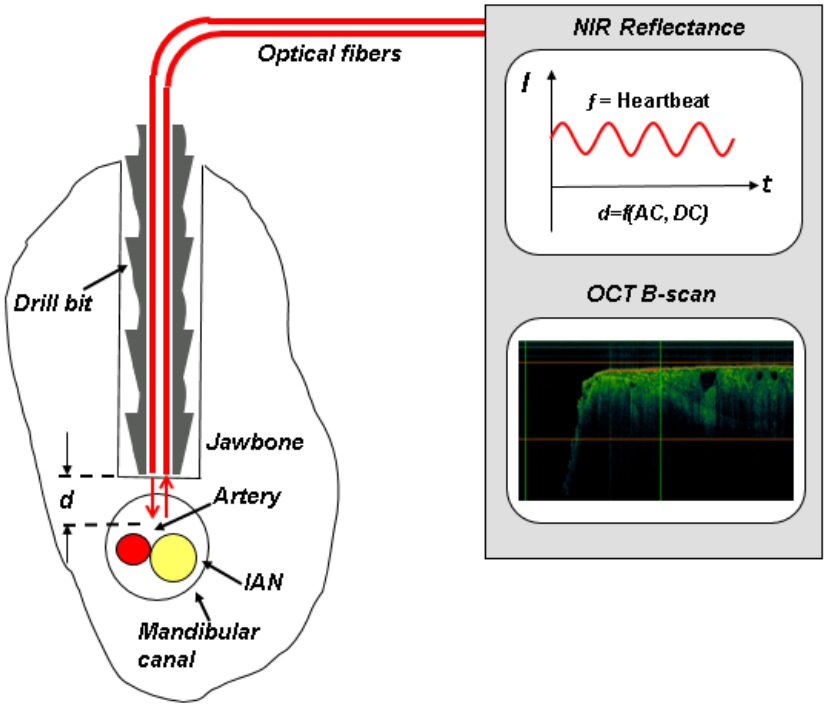

Fig. 2. "Smart drill" concept using a bimodal NIR and OCT approach (Patent pending: US 2012/0271176 A1).

2. Materials and methods

2.1 Phantoms for NIR studies

Water-based liquid phantoms were chosen for blood simulation in order to be able to circulate the phantoms through an artery-simulating tube using a pump. Liquid phantoms were also used to simulate the surrounding trabecular bone tissue due to the ease of embedding the arterial tube at varying positions, as well as to ensure a flexible medium to enable the artery phantom to move in a pulsatile fashion (rather than a solid phantom, in which the tube would not move). Additional advantages of liquid phantoms include the simplicity of fabrication and manipulation of optical properties [19]. The phantoms consisted of Intralipid® 20%

#197910 - $15.00 USD Received 19 Sep 2013; revised 15 Nov 2013; accepted 18 Nov 2013; published 2 Dec 2013

(Fresenius Kabi Italia, Italy) for scattering and Higgins Waterproof Drawing Ink (Black India, Item 44201, Sanford, USA) for absorption. They were designed to represent the optical properties of bone [20, 21] and arterial blood [22, 23] at the wavelength of the illumination laser (852nm), details shown in Table 1. Previous work in Intralipid and ink phantoms informed the phantom recipes [19]. The bone phantoms were characterized with our in house phantom characterization system [24, 25] after fabrication (right column, Table 1). The blood phantoms were too highly absorbent for standard characterization, however are assumed to match the targeted values based on linear extrapolation of the recipes.

Table 1. Phantom optical properties at 850nm

	Literature	*Phantom*
Arterial blood phantom		
Absorption (μ_a, cm^{-1})	5.6[a]	5.7[e] (Target recipe)
Reduced scattering (μ_s', cm^{-1})	11-21 at 633nm[b]	7.1[e] (Target recipe)
Bone phantom		
Absorption (μ_a, cm^{-1})	~0.08[c]-0.2[d]	0.15 (Measured)
Reduced scattering (μ_s', cm^{-1})	~11-13[c]	11.4 (Measured)

[a] Calculated from 98% HbO2 [23].
[b] [22].
[c] [20].
[d] [21].
[e] [19].

For bimodal measurements, a 15% weight by volume gelatin-based phantom was fabricated. Gelatin was chosen as a medium since the refractive index, a key parameter for accurate OCT thickness measurements, is closer to tissue (~1.36 for 15% weight by volume gelatin, vs. 1.33 for liquid phantoms and ~1.4 for tissue). The gelatin phantom was fabricated with bone optical properties using the same recipe as above for the liquid phantoms after verification in a spectrometer that the cured gelatin alone contributed insignificantly to the absorption and scattering at 850nm.

2.2 Experimental setup for NIR measurements

An *in vitro* setup was built for phantom experiments with the following hardware: a pulsatile pump, cardiac pressure gauge for a reference frequency signal, and an avalanche photodiode (APD) with customized detection electronics (Fig. 3, Table 2).

#197910 - $15.00 USD Received 19 Sep 2013; revised 15 Nov 2013; accepted 18 Nov 2013; published 2 Dec 2013

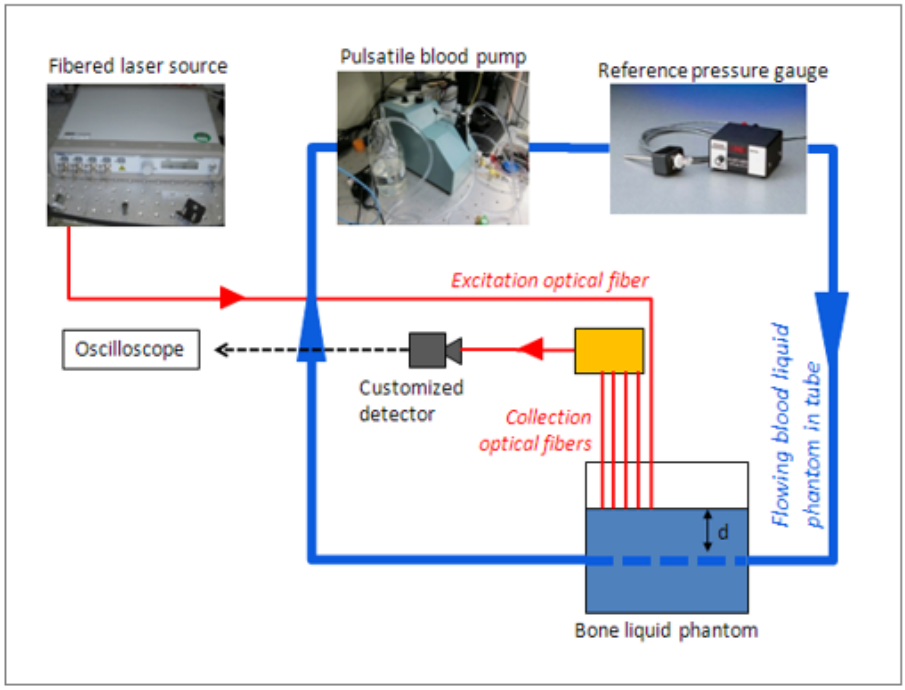

Fig. 3. NIR measurement setup for simulating a pulsing artery embedded in bone phantom, using a cardiac pulsatile pump, silicone tubes and liquid tissue-simulating phantoms. A fibered laser source sends light to the sample and a fiber probe with multiple source-detector separation options (collection optical fibers) collects the light and sends it to the customized detector, whose signal is recorded on an oscilloscope.

Table 2. NIR *in vitro* setup equipment

Equipment	***Brand***	***Model***
APD with customized detection board	In-house	
Fiber-coupled laser source	Thorlabs	MCLS1
Oscilloscope	Tektronix	TDS2024B
Pulsatile blood Pump	Harvard Apparatus	PY2 55-1838
Blood pressure transducer	Harvard Apparatus	MA1 72-4496
Optical power meter	Newport	1030-C
Optical power sensor	Newport	818-SL
Laser micro-meter	Keyence	IG-028

A fibered laser provides approximately 9mW of 852nm light (a wavelength with strong oxy-hemoglobin absorption) at the output of the source fiber. 1-3μW is detected after the detector fibers with a tissue-simulating phantom in contact with the probe. A custom five-fiber probe, shown in Fig. 4, was designed and built in-house for multiple source-detector distance measurement capability. The probe consists of five 600μm core diameter fibers in a fixed linear geometry with center-to-center distances of approximately 650μm (range 630-699μm). Although in the final application the probe must fit within a 2mm space within the drill, five fibers were initially chosen to explore the effects of different source-detector separations. However, not enough signal was seen in the last fiber in these experiments and only the closest three fiber pairs were used to explore center-to-center source-detector separations of 630, 1329 and 1973μm. The first fiber is used as a source channel and the remaining fibers are used separately as detection channels depending on which fiber was

#197910 - $15.00 USD Received 19 Sep 2013; revised 15 Nov 2013; accepted 18 Nov 2013; published 2 Dec 2013

connected to the detector. The phantom chamber consists of a container with a 1.6mm inner diameter and 3.2mm outer diameter silicone Tygon tube passing through it. The 1.6mm diameter tube is representative of the actual size of the IAN artery, based on data from two references: the first measures the IAN artery at 1.4-1.5mm in edentulous subjects and 1.7-2mm in dentate subjects [4] and the second reference measures the IAN artery at 1.84 ± 0.6mm [5]. The tube was measured during pulsation with a laser micrometer to determine its displacement and it was found to vary by about 0.2mm in diameter, or about 6.25%. The true value of the percent change of the IAN artery was not found in the literature; however the reported value for the larger carotid artery diameter change during pulsation is 13% [26]. During an experiment, the bone-simulating phantom sits in the container, around the tube, while the blood phantom circulates through the tube. The cardiac pump provides heart-beat-like pulsatility. Settings were adjusted to ensure 1-1.5Hz pulse rate. To monitor the reference pulse, a pressure gauge (Harvard Apparatus) made specifically for cardiac-type signals and for the range of pressures created by the pump was used. The raw (AC + DC) signal was fed to an oscilloscope to record the data. An example trace of the reference pulse and an optical signal is shown in Fig. 5.

A custom, in-house detector using a Si APD detection circuit board with very low bandwidth (10Hz) and noise (SNR = 110dB) was built to overcome the challenge of measuring the weak cardiac pulse signal from a depth within tissue.

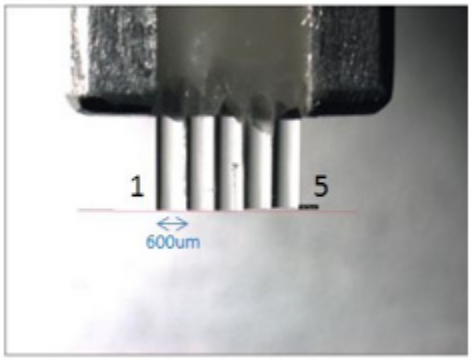

Fig. 4. Fiber optic probe for NIR experiments. The fibers are each 600μm core diameter and fixed next to each other with a center-to-center distances of approximately 650μm. Typically fiber 1 is used as the source channel, and one of the remaining fibers can be used as the detection channel.

#197910 - $15.00 USD Received 19 Sep 2013; revised 15 Nov 2013; accepted 18 Nov 2013; published 2 Dec 2013

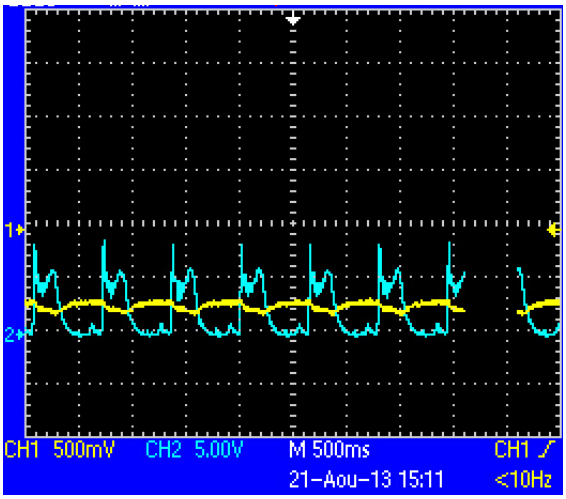

Fig. 5. A sample oscilloscope screenshot of the raw pulse signal (yellow, CH1), and reference signal from the pressure gauge (cyan, CH2), showing the cardiac-simulated pressure generated by the pump and detected by the probe. Horizontal axis: time, 500ms per division.

Experiments were performed with the system and phantoms described above according to the following general procedure:

1. The probe was positioned in contact with the tube (before adding the bone phantom, for visibility) so that pulsation did not create any space between the probe and tube, but also so that the probe was not pressed into the tube.
2. Bone phantom was added around the tube, covering the probe up to a depth of ~6mm.
3. Data for each source-detector separation was separately acquired at 0.5mm increments by moving the probe away from the tube, covering a range of 0mm (contact) to 3.5-4mm from the tube.

2.3 Ex vivo jaw bone sample for OCT

A human cadaver mandible (International Biologics, Inc.) was used. The mandible had no external soft tissues remaining and was treated for prolonged conservation as per the vendor's standard procedure, including cleaning with bio-salts and drying via natural residue. For the measurements presented here, the nervovascular bundle was left intact inside the canal. One sample is shown in Fig. 6, although for this sample, the bundle had been removed for visualization of the canal geometry. Samples were prepared for imaging as follows:

1. Sections of the full human jaw bone were cut to get a 1 cm section along the length of the IAN canal.
2. On this piece, the bone side was thinned with a file to leave a thin wall between the outside surface and the nerve bundle's channel. This way, the purely cortical bone layer was removed and the internal trabecular bone was exposed, to reproduce the input surface an IAN sensor probe would see in a real procedure.
3. This thin wall was filed to form a wedge with wall thicknesses from about 0.1 to 1.3 mm above the IAN canal.

#197910 - $15.00 USD Received 19 Sep 2013; revised 15 Nov 2013; accepted 18 Nov 2013; published 2 Dec 2013

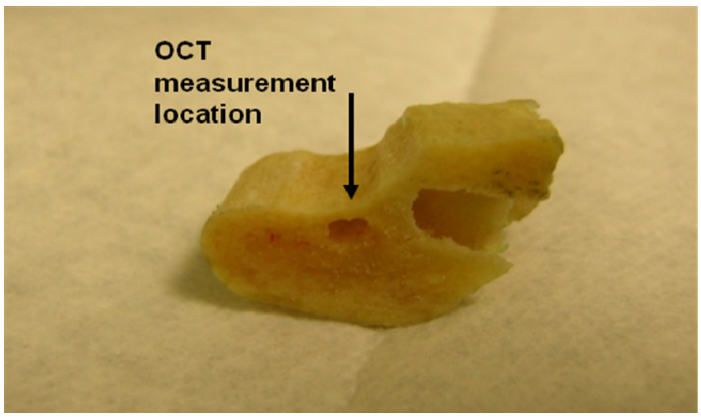

Fig. 6. Picture of one human mandible sample used in the OCT measurements (shown with neurovascular bundle removed). The OCT measurement was taken as indicated just above the mandibular canal (the hole under the black arrow) where the IAN neurovascular bundle is located. The bone was filed into a taper shape to give varying thickness of bone tissue above the canal.

2.4 Experimental setup for OCT measurements

OCT measurements were performed with a Thorlabs Swept Source OCT system (Thorlabs, model OCS1300SS, Newton, NJ). This system provides the capability for standard structural OCT imaging. It operates at a central wavelength of 1325 nm (bandwidth ~100 nm), with an average output power of ~10 mW.

3. Results and discussion

3.1 NIR results

Data for each distance to the artery-simulating tube and each source-detector separation were compiled both for AC (peak-to-peak amplitude) and DC (mean raw signal) captured signals. Figure 7 shows the relative AC and DC amplitudes for all measurement conditions, including 9 distances from the probe to the tube, from 0mm (contact) to 4mm, in steps of 0.5mm, and all three center-to-center source-detector fiber separations: 630, 1329 and 1973μm.

#197910 - $15.00 USD Received 19 Sep 2013; revised 15 Nov 2013; accepted 18 Nov 2013; published 2 Dec 2013

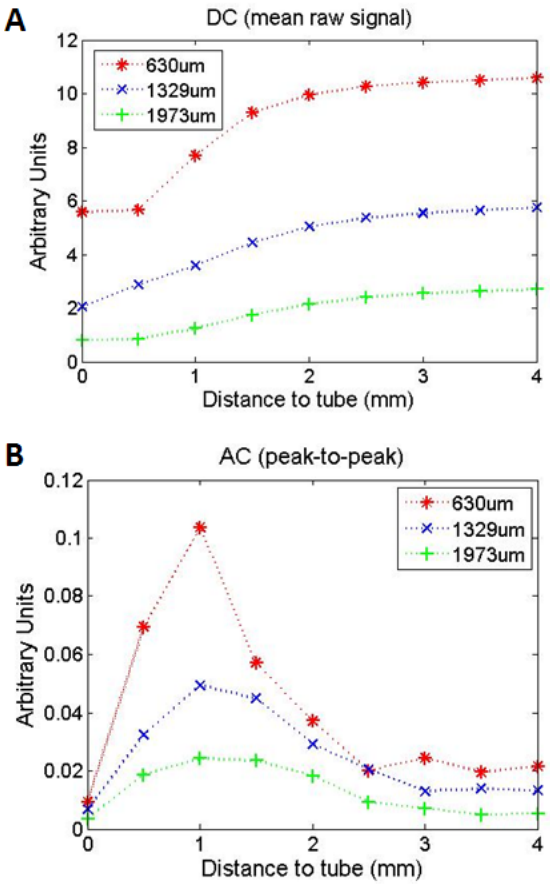

Fig. 7. DC (mean raw signal) (A) and AC (peak-to-peak amplitude) (B) vs. distance from probe to tube for different source-detector separations.

Figure 7(A) shows the mean raw DC signals for each source-detector separation. From this data, a trend can be identified: the smallest source-detector separation (630μm, in red) has the sharpest slope and plateaus closest to the tube, around the 2mm distance, while the largest source-detector separation (1973μm, in green) has the most shallow slope and plateaus further from the tube, continuing to provide contrast to changes in distance through approximately the 3mm measurement. Empirically, these trends make sense: the closer the probe is to an absorbing artery, the lower the reflectance back into the probe will be. Shorter source-detector separations are sensitive to shallower depths [27], and therefore to closer probe-tube distances. This contrast could be used in a long range neurovascular bundle proximity sensor, since the reflectance decreases as the probe approaches several millimeters from the artery.

The AC amplitudes shown in Fig. 7(B) for all three source-detector separations follow a similar trend. The AC amplitude is minimal when far from the tube, >3mm. As the probe approaches the tube, the AC amplitude increases to a peak, then decreases again to a minimum when the probe is in contact with the tube. This trend is visible for all data taken. Monte Carlo simulations are needed to fully explain the trend, and are currently under investigation. However, this trend of the AC signal is consistent with previously published experimental and Monte Carlo results using a pulsatile tube phantom to investigate the influence of artery depth on pulse oximeter signal strength [28]. The previously published

#197910 - $15.00 USD Received 19 Sep 2013; revised 15 Nov 2013; accepted 18 Nov 2013; published 2 Dec 2013

work used a much larger geometry (11mm source-detector separation and 1.2-6.8mm diameter tubes), saw deeper AC peaks and larger FWHM (e.g. at 2.5mm, FWHM ~4.5mm), consistent with the trend we see here that larger source-detector separations are most sensitive at deeper tube locations and with broader depth sensitivity.

An empirical explanation of the current results and previously published Monte Carlo simulation results using the interrogation volume can be considered. The relative change in volume due to a pulsation should be 1) at first small when the probe is far from the pulsing tube since the pulsing volume consumes less of the volume of interrogation, 2) then at a peak at some distance where the pulsing tube sits in an optimal position within the volume of interrogation, and finally 3) the signal will decrease again as the probe approaches the absorbing tube: less of the volume of interrogation is displaced by the pulse. The AC signals show that the smaller source-detector separation of 630μm has a shallower and narrower peak than the larger 1973μm separation.

For this work, only relative proximity to the neurovascular bundle was considered. Calibration methods are being explored to quantify the distance. By creating lookup tables of the AC signal, DC signal and distance using a known calibration data set, we can fit distance to a new set of AC and DC values. However, implementation of this method in vivo, outside of the phantom context, will be complicated by patient-to patient variation in optical properties, bleeding during drilling and any other factors influencing the raw reflectance. Relative ranging may be sufficient for the current application since the position of the AC peak, and more specifically the drop in AC amplitude as the probe approaches contact, appear to be reproducible at ~1mm from the tube across a variety of measurement conditions including 3 source detector separations, a ~3x larger diameter tube (not shown), and a bone phantom absorption of ~100x higher than normal bone properties (not shown). This peak and AC amplitude decrease could be used in a first step to approach the neurovascular bundle, bringing the surgeon to approximately 1mm from the bundle and potentially reducing the required "safety zone" from 2mm to 1mm (further reduction may be possible when combined with OCT, see results below).

3.2 OCT results

B-mode scans were performed on the *ex vivo* human mandible after it was cut into a wedge to show differing depths through bone to the IAN neurovascular bundle. Figure 8 shows such a scan, with the tapered surface placed horizontally at the top of the image so that the left side shows a shallow canal and IAN bundle, and moving to the right, the canal and bundle plunge deeper as indicated by white arrows. The overall thickness of the tissue section was calculated using Thorlabs software with a refractive index of 1.4. From this image, we identify the border of jaw bone and the mandibular canal for the first ~0.6-0.8mm of the image total thickness as it plunges in depth relative to the surface from left to right. As it descends further, image contrast decreases, however the border between the bone and bundle is still visible intermittently.

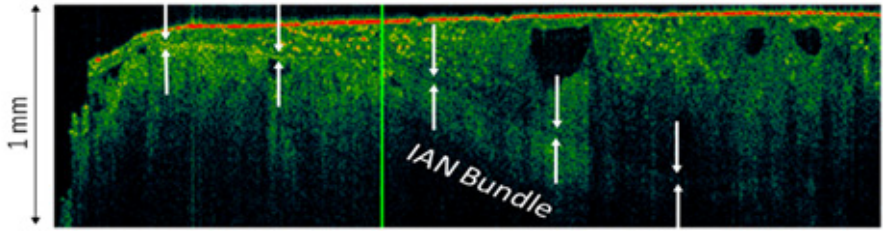

Fig. 8. An SS-OCT B-scan of the tapered jaw bone, with the tapered edge placed horizontally at the top of the image so that the mandibular canal and IAN descend in depth from left to right. The position of the first surface of the canal containing the IAN neurovascular bundle is indicated by the white arrows.

#197910 - $15.00 USD Received 19 Sep 2013; revised 15 Nov 2013; accepted 18 Nov 2013; published 2 Dec 2013

Because of the low contrast between the tissue types (bone, nerve, and artery), interpretation of the data and assessment of the interface position is impractical for real time acquisition in A-mode (point measurement) and requires at minimum a B-mode image, as above. Contrast enhancement techniques are under investigation to improve the readability of both A and B scans at depths greater than ~0.6-0.8mm. Using a longer wavelength, e.g. 1.5-1.8μm instead of 1.3μm, will likely improve depth penetration, however currently availability of sources at these wavelengths is limited. Signal processing contrast enhancement methods may improve the ability to distinguish the tissue types.

3.3 Bimodal phantom results

Preliminary bimodal NIR and OCT data were taken on the same gelatin phantom at 1mm thickness above the embedded artery-simulating tube. Photos of each modality setup and results are presented in Fig. 9(A), 9(C), OCT and NIR, respectively, below.

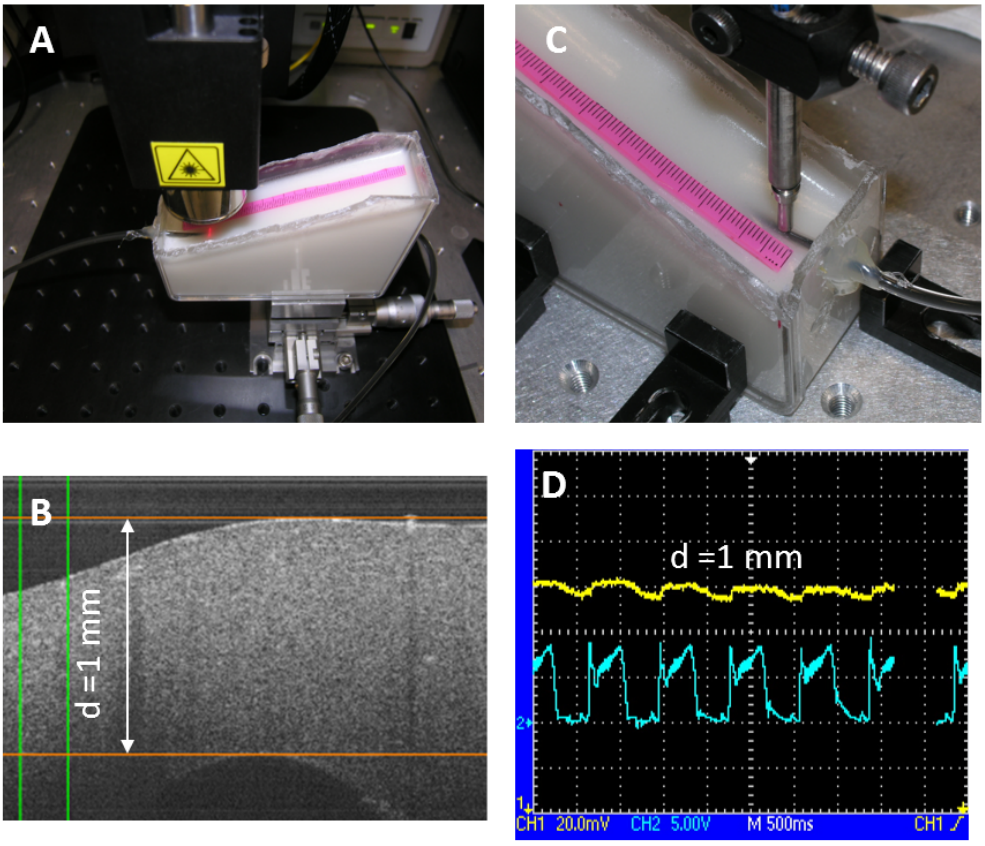

Fig. 9. Bimodal data. OCT: A: measurement scheme, B: sample data at 1mm phantom thickness over artery-simulating tube. NIR: C: measurement scheme, D: NIR 650nm source-detector separation pulse data at the same position as the OCT measurement, 1mm thickness over the artery-simulating tube: top curve (yellow) and reference pressure gauge signal bottom curve (cyan).

Figure 9(B) shows the OCT B-scan cross section of the gelatin phantom over the artery-simulating tube. The surface of the tube is just visible under 1mm of bone-simulating phantom. The thickness was calculated using a refractive index of 1.36. Figure 9(D) shows the pulse from the artery-simulating phantom at the same 1mm thickness position. This data represents the approximate thickness at which the NIR AC signal is at a peak and the OCT is

#197910 - $15.00 USD Received 19 Sep 2013; revised 15 Nov 2013; accepted 18 Nov 2013; published 2 Dec 2013

reaching its limit of depth penetration. Currently, these measurements are performed consecutively, using a ruler as a fiducial marker to match the positions (on the surface of the gelatin phantom in pink in Fig. 9(A), 9(C)). Development of a bimodal fiber probe will facilitate future bimodal studies (See Conclusions and Future Work, section 4).

3.4 Concept of operation of a bimodal "smart drill"

The techniques above could eventually be integrated into a bimodal (NIR + OCT) "smart drill" used for guidance during implant placement. Based on the results, one envisioned concept of operation could be as follows:

1. Using appropriate traditional pre-operative imaging, such as radiography or CBCT (as discussed in the Introduction), the procedure starts as usual by approaching the recommended "safety zone" of 2-4mm from the mandibular canal.
2. As the drill approaches the "safety zone," the NIR DC signal begins to decrease (below approximately 3mm).
3. Drilling continues until the NIR AC signal peaks and begins decreasing (~0.5-1.5mm range), bringing the surgeon past the previously required "safety zone." (It could also be imagined that by using two different source-detector distances, the sensor could see the AC signal of the larger distance decrease first, followed by the shorter distance).
4. Finally, OCT takes over as the primary modality for final channel depth determination: a B-mode image will qualitatively guide the drill to the proximity of the canal / neurovascular bundle (approximately in the <0.8mm range).

Depending on the accuracy of placement using this technique, which will need to be analyzed in pre-clinical work, the required "safety zone" could be reduced from 2 to 4mm to less than 1mm, optimizing the use of available bone volume for improved osseointegration and minimizing the risk of damage to the IAN.

4. Conclusions and future work

Proof of concept has been established for using NIR absorption to sense proximity to simulated artery pulsations in a phantom model and OCT to visualize the location of the mandibular canal in an *ex vivo* human mandible, towards the ultimate goal of sensing the proximity to a neurovascular bundle. Two separate sources of NIR sensitivity to the distance of the target were found: the pulsatile signal generated by a model artery as well as the DC absorption difference of a blood phantom vs. bone phantom each showed contrast to the proximity of the pulse. These results hold true across the two different tube diameters tested (data for larger tube not shown). OCT results demonstrate a third and complementary source of sensitivity to the location of a neurovascular bundle. By combining NIR results with OCT imaging results, the two methods together may provide complete ranging information over the scale of 0.5-3mm (NIRS) and 0-0.8mm (OCT). This technique has the potential to overcome many of the disadvantages of currently available methods, enabling real-time, non-ionizing and high resolution placement of dental implants.

Ongoing and future work is focused on *ex vivo* and/or *in vivo* validation experiments and integrating both modalities into a common fiber probe. Exhaustive bimodal *ex vivo* tissue studies are currently in progress. Development of the bimodal fiber probe is underway and remains as a major step towards clinical implementation. The NIR modality is already fibered and forward-looking fibered measurements are possible with OCT. We are currently working on integrating them into small probe and drill bit configurations. We are currently developing Monte Carlo simulations for the NIR experiments that, along with phantom tests, will let us explore possible effects of optical property variations due to pooling of blood during drilling, and intermittently during washing, off axis positioning errors and other possible in situ

#197910 - $15.00 USD Received 19 Sep 2013; revised 15 Nov 2013; accepted 18 Nov 2013; published 2 Dec 2013

measurement complications. Contrast and depth penetration enhancement techniques are also under consideration for improving the OCT results.

Acknowledgments

The authors thank Alex Vitkin and Brett Bouma for discussions on contrast enhancement for OCT.

#197910 - $15.00 USD Received 19 Sep 2013; revised 15 Nov 2013; accepted 18 Nov 2013; published 2 Dec 2013